

Modeling Intra-Cluster Gas in Triaxial Dark Halos : An Analytic Approach

JOUNGHUN LEE AND YASUSHI SUTO

Department of Physics, The University of Tokyo, Tokyo 113-0033, Japan

lee@utap.phys.s.u-tokyo.ac.jp, suto@phys.s.u-tokyo.ac.jp

ABSTRACT

We present the first physical model for the non-spherical intra-cluster gas distribution in hydrostatic equilibrium under the gravity of triaxial dark matter halos. Adopting the concentric triaxial density profiles of the dark halos with constant axis ratios proposed by Jing & Suto (2002), we derive an analytical expression for the triaxial halo potential on the basis of the perturbation theory, and find the hydrostatic solutions for the gas density and temperature profiles both in isothermal and polytropic equations of state. The resulting iso-potential surfaces are well approximated by triaxial ellipsoids with the eccentricities dependent on the radial distance. We also find a formula for the eccentricity ratio between the intra-cluster gas and the underlying dark halo. Our results allow one to determine the shapes of the underlying dark halos from the observed intra-cluster gas through the X-ray and/or the Sunyaev-Zel'dovich effects clusters.

Subject headings: cosmology:theory – dark matter – galaxies: clusters: general – X-ray: galaxies

1. INTRODUCTION

While clusters of galaxies are regarded as one of the most important cosmological probes, the conventional modeling of the intra-cluster gas is very approximate at best. The most popular and traditional description is the spherical isothermal β model, which has been claimed as a good empirical description for the observed intra-cluster gas, and in fact has been widely used in practically almost all statistical analyses of galaxy clusters including mass, temperature and luminosity functions, and the Hubble constant (or more precisely the angular diameter distance) measurement via the Sunyaev-Zel'dovich (SZ) effect (e.g., Birkinshaw 1999, for a review).

The situation is changing rapidly both observationally and theoretically; recent X-ray satellites such as *Chandra* and *XMM-Newton* have greatly improved the angular-resolution and the statistical reliability of X-ray maps of galaxy clusters, and often detected the significant departure from the isothermality and the non-sphericity of the intra-cluster gas. Buote et al. (2002), for instance, reported evidence from the *Chandra* observation for a flattened triaxial dark matter halo around the elliptical galaxy NGC720 (see also, Romanowsky & Kochanek 1998). In the radio band the bolometer array technique improved the angular resolution of the cluster SZ map. One successful example is the discovery of substructure of the most luminous X-ray cluster RX J1347-1145 by Komatsu et al. (2001), which was subsequently confirmed with *Chandra* (Allen et al. 2002).

The theoretical understanding of dark matter halos is also advanced significantly. The spherical averaged density profiles of dark halos are known to be well approximated by a sequence of universal density profiles (Navarro, Frenk & White 1996, 1997; Fukushige & Makino 1997; Moore *et al.* 1998; Jing & Suto 2000). The importance of non-spherical effects on the mass function of dark halos was first raised by Monaco (1995), and then studied analytically (Audit, Teyssier, & Alimi 1997; Lee & Shandarin 1998), and in detail with numerical simulations (Lee & Shandarin 1999; Sheth & Tormen 1999; Jenkins et al. 2001). More importantly, the systematic effect of the non-sphericity of intra-cluster gas on the estimate of the Hubble constant from the SZ observations is well recognized (Birkinshaw, Hughes, & Arnaud 1991; Inagaki, Suginozawa & Suto 1995; Yoshikawa, Itoh & Suto 1998; Hughes & Birkinshaw 1998; Fox & Pen 2002). In particular the recent work of Jing & Suto (2002) showed that the simulated halos are well approximated by a sequence of the concentric triaxial distribution with their axis directions being fairly aligned. This naturally opens a possibility to compute the hydrostatic equilibrium solution of the intra-cluster gas under the gravity of the triaxial dark matter halos. Generalizing the prescription of Makino, Sasaki & Suto (1998) and Suto, Sasaki, & Makino (1998) who obtained the hydrostatic equilibrium solution for the spherical halo profiles, we find a series of analytical solutions for gas embedded in the triaxial halo profiles. In the present paper, we focus on the mathematical aspects of the problem, and their astrophysical applications (weak/strong lensing, SZ and X-ray observations) will be described elsewhere.

The rest of the paper is organized as follows: In §2 we briefly outline the procedure to compute gas and temperature profiles in hydrostatic equilibrium with gravitational potential of dark matter halos. In §3 we present the analytical derivation of the triaxial halo potential using the perturbation theory, and describe the shapes of the iso-potential surfaces. The analytical and numerical results for the gas density and temperature profiles are summarized in §4, and §5 is devoted to conclusions and discussion. In Appendix, we provide the detailed analytical expressions of our perturbative results.

2. DISTRIBUTION OF INTRA-CLUSTER GAS IN HYDROSTATIC EQUILIBRIUM

If the intra-cluster gas embedded in the dark matter halo is in hydrostatic equilibrium, its distribution is described by

$$\frac{1}{\rho_g} \nabla P_g = -\nabla \Phi, \quad (1)$$

where Φ is the gravitational potential of the system, and ρ_g and P_g represent the density and the pressure of the intra-cluster gas, respectively. In what follows, we neglect the contribution of the gas and stellar masses, and assume that the gravitational potential of the total system is well approximated by that of the halo (Suto, Sasaki & Makino 1998).

Once the equation of state for the intra-cluster gas and the density profile of the dark matter halo are given, then the density and temperature profiles of intra-cluster gas are obtained by solving equation (1). Although the intra-cluster gas is commonly assumed to be isothermal, it has been recently claimed that the intra-cluster gas might be better described as polytropic (Markevitch *et al.* 1998; Komatsu & Seljak 2001). Thus we consider both isothermal and polytropic cases.

Consider first the isothermal gas with an equation of state:

$$P_g = K \rho_g, \quad K \equiv \frac{k_B T_g}{\mu m_p}, \quad (2)$$

where T_g , k_B , μ , and m_p denote the (constant) gas temperature, the Boltzmann constant, the mean molecular weight, and the proton mass, respectively. In this case the hydrostatic equilibrium equation (1) is easily solved to yield

$$\frac{\rho_g}{\rho_{g0}} = \exp \left[-\frac{1}{K} (\Phi - \Phi_0) \right], \quad (3)$$

where Φ_0 is an integration constant that can be fixed by the condition of $\rho_g(r = 0) = \rho_{g0}$. Note that the value of Φ_0 depends on the value of K .

Turn next to the polytropic model with an equation of state:

$$P_g = K_0 \rho_g^\gamma, \quad K_0 \equiv \frac{k_B T_{g0}}{\mu m_p}, \quad (4)$$

where $\gamma (\neq 1)$ is the polytropic index, and T_{g0} is the value of the gas temperature at $r = 0$. In this polytropic model, the gas temperature is not constant but proportional to $\rho_g^{\gamma-1}$. So, in this case, equation (1) reduces to

$$\nabla(\rho^{\gamma-1}) = -\frac{\gamma-1}{K_0 \gamma} \nabla \Phi, \quad (5)$$

whose solution is derived as

$$\frac{T_g}{T_{g0}} = \frac{1 - \gamma}{K_0 \gamma} (\Phi - \Phi_0), \quad \frac{\rho_g}{\rho_{g0}} = \left[\frac{1 - \gamma}{K_0 \gamma} (\Phi - \Phi_0) \right]^{1/(\gamma-1)}. \quad (6)$$

Thus, the general density and temperature profiles of intra-cluster gas in both isothermal and polytropic cases can be straightforwardly obtained in terms of the gravitational potential of the underlying halo. Furthermore, equations (3) and (6) also imply that the iso-potential surfaces of the triaxial dark halo coincide with the iso-density surfaces of the intra-cluster gas. This is simply a direct consequence of *X-ray shape theorem* (Buote & Canizares 1994; Buote et al. 2002); the hydrostatic equilibrium equation (1) yields

$$\nabla P_g \times \nabla \Phi = \nabla \rho_g \times \nabla \Phi = 0. \quad (7)$$

Moreover, with the polytropic equation of state (eq. [4]), the gas temperature also satisfies

$$\nabla T_g \times \nabla \Phi = 0. \quad (8)$$

Therefore, the gas density, temperature, and pressure are constant on the iso-potential surfaces at the same time. In consequence, the gravitational potential is the central quantity for the hydrostatic gas model. In the following section we derive an analytical expression for the triaxial dark halo potential, and study the general properties of the resulting iso-potential surfaces.

3. GRAVITATIONAL POTENTIAL OF TRIAXIAL DARK HALOS

3.1. Triaxial Density Profile of Dark Halos

In what follows, we adopt the following concentric triaxial density profile for the dark matter halos (Jing & Suto 2002):

$$\rho(R) = \frac{\delta_c \rho_{\text{crit}}}{(R/R_0)^\alpha (1 + R/R_0)^{3-\alpha}}, \quad (9)$$

where R_0 is the scale length, δ_c is the dimensionless characteristic density contrast with respect to the critical density ρ_{crit} of the universe at the present epoch, and α represents the inner slope of the density profile. Note that equation (9) is identical to the one which describes the spherical density profile (Navarro, Frenk & White 1997; Fukushige & Makino 1997; Moore *et al.* 1998) except that the spherical radius r is replaced by the the major axis length R of the iso-density surfaces :

$$R^2 = a^2 \left(\frac{x^2}{a^2} + \frac{y^2}{b^2} + \frac{z^2}{c^2} \right), \quad (a \geq b \geq c). \quad (10)$$

The N-body simulations by Jing & Suto (2002) imply that the best-fit values of α are $\alpha = 1$ and $\alpha = 3/2$ for cluster and galactic-scale halos, respectively. Thus we pay particular attention to these two cases.

We quantify the ellipsoidal shape of a *halo* iso-density surface by defining the two eccentricities:

$$e_b \equiv \sqrt{1 - \left(\frac{b}{a}\right)^2}, \quad e_c \equiv \sqrt{1 - \left(\frac{c}{a}\right)^2}, \quad (11)$$

and $a \geq b \geq c$ implies $e_b \leq e_c$. The values of e_σ^2 ($\sigma = b, c$) measure the degree of the deviation of the ellipsoidal iso-density surfaces from the spherical ones along the corresponding principal axis direction.

3.2. Perturbative Expansion of the Triaxial Halo Potential

The gravitational potential of a dark halo with the triaxial density profile (eq.[9]) can be written as (Binney & Tremaine 1987)

$$\Phi(\mathbf{r}) = -\pi G \left(\frac{bc}{a}\right) \int_0^\infty \frac{[\psi(\infty) - \psi(m)]}{\sqrt{(\tau + a^2)(\tau + b^2)(\tau + c^2)}} d\tau, \quad (12)$$

$$\psi(m) = 2 \int_0^m \rho(R) R dR, \quad (13)$$

$$m^2 = a^2 \left(\frac{x^2}{a^2 + \tau} + \frac{y^2}{b^2 + \tau} + \frac{z^2}{c^2 + \tau} \right), \quad (14)$$

where $\mathbf{r} = (x, y, z) = r(\sin \theta \cos \phi, \sin \theta \sin \phi, \cos \theta)$, and τ labels the iso-potential surfaces on which $m = m(\mathbf{r}, \tau)$ is constant. While numerical integration is required in general to obtain the triaxial gravitational potential with equations (9) to (14), small eccentricities ($e_b^2 \leq e_c^2 \ll 1$) cases enable us to approach this problem analytically with the perturbative expansion.

The theory for the ellipsoidal perturbation of the spherical systems has a long history (e.g., see Jeffreys 1976, and references therein). In performing the ellipsoidal perturbation, there are two different ways to arrange the perturbed terms. One is the equal-volume approach: the perturbed ellipsoids have the same volumes as the unperturbed original spheres. The other is the equal-length approach: the perturbed ellipsoids and the unperturbed spheres have the same length scales. For instance, one can force the major axis lengths of the perturbed ellipsoids to be same as the radii of the original spheres. The two approaches differ only in arranging the perturbed ellipsoidal terms, and the perturbation theory is basically

the same either way. Though the equal-volume approach is more conventional, we take the equal-length approach here, for which the reason is as follows.

We develop the perturbation theory here mainly to provide an ellipsoidal correction to the conventional spherical modeling of the observed clusters. What is observationally measurable, however, is not the volumes but the length scales of the clusters. For example, in SZ observations, the cluster length scales in the direction perpendicular to the line-of-sight are measured. In the standard spherical model, this tangential length scales are taken as the spherical radii of the clusters. In ellipsoidal model, however, the same tangential length scales are no longer same as the line-of-sight length. Thus, in the two models, the volumes of the clusters are not the same. Thus, given the future application of the perturbation theory to the observed clusters, we perform the perturbative expansion of the gravitational potential in such a way that the perturbed ellipsoids have the same length scales (here, the major axis lengths) as the radii of the spheres but do not have the same volumes. Derivation of the perturbative expansion of $\Phi(\mathbf{r})$ up to the first order of e_σ^2 in this way proceeds as follows.

First, $\psi(m)$ defined in equation (13) for the given triaxial density profile $\rho(R)$ in equation (9) is analytically given as

$$\psi(m) = \frac{2R_0^2 \delta_c \rho_{\text{crit}}}{2 - \alpha} \left(1 + \frac{R_0}{m}\right)^{\alpha-2}. \quad (15)$$

Expressing b and c in terms of a as $b = a\sqrt{1 - e_b^2}$ and $c = a\sqrt{1 - e_c^2}$ by equation (11), we expand m in equation (14) with respect to e_b^2 and e_c^2 to their first order:

$$m \approx m_{sp} \left(1 + \frac{m_{sp}^2}{r^2} \frac{e_b^2 \sin^2 \theta \sin^2 \phi + e_c^2 \cos^2 \theta}{2}\right), \quad (16)$$

where $m_{sp} \equiv ar/\sqrt{a^2 + \tau}$ is the value of m for the spherical case ($e_b = e_c = 0$).

Equations (15) and (16) yield the first order approximation of $\psi(m)$:

$$\psi(m) \approx 2R_0^2 \delta_c \rho_{\text{crit}} \left(1 + \frac{R_0}{m_{sp}}\right)^{\alpha-2} \left(\frac{1}{2 - \alpha} + \frac{R_0}{m_{sp} + R_0} \frac{m_{sp}^2}{r^2} \frac{e_b^2 \sin^2 \theta \sin^2 \phi + e_c^2 \cos^2 \theta}{2}\right). \quad (17)$$

Similarly, we approximate $\sqrt{(\tau + a^2)(\tau + b^2)(\tau + c^2)}$ and bc/a in equation (12) as

$$\sqrt{(\tau + a^2)(\tau + b^2)(\tau + c^2)} \approx \frac{m_{sp}^3}{a^3 r^3} \left(1 + \frac{m_{sp}^2}{r^2} \frac{e_b^2 + e_c^2}{2}\right), \quad \frac{bc}{a} \approx a \left(1 - \frac{e_b^2 + e_c^2}{2}\right). \quad (18)$$

Now that all the quantities in the integral of equation (12) are expressed in terms of m_{sp} as equations (16) to (18), we change the integration variable from τ to m_{sp} , and perform

the integration of equation (12) to obtain the following 1st-order approximation for Φ :

$$\Phi(\mathbf{u}) \approx C \left[F_1(u) + \frac{e_b^2 + e_c^2}{2} F_2(u) + \frac{e_b^2 \sin^2 \theta \sin^2 \phi + e_c^2 \cos^2 \theta}{2} F_3(u) \right], \quad (19)$$

where $\mathbf{u} \equiv \mathbf{r}/R_0$, and $C = 4\pi G \delta_c \rho_{\text{crit}} R_0^2$, and the three functions, $F_1(u)$, $F_2(u)$, and $F_3(u)$ are defined as

$$F_1(u) \equiv \frac{1}{\alpha - 2} \left[1 - \frac{1}{u} \int_0^u \left(\frac{t}{t+1} \right)^{2-\alpha} dt \right], \quad (20)$$

$$F_2(u) \equiv \frac{1}{\alpha - 2} \left[-\frac{2}{3} + \frac{1}{u} \int_0^u \left(\frac{t}{t+1} \right)^{2-\alpha} dt - \frac{1}{u^3} \int_0^u \frac{t^{4-\alpha}}{(t+1)^{2-\alpha}} dt \right], \quad (21)$$

$$F_3(u) \equiv \frac{1}{u^3} \int_0^u \frac{t^{4-\alpha}}{(t+1)^{3-\alpha}} dt. \quad (22)$$

Equation (19) is valid for any arbitrary value of α . For the interesting values of $\alpha = 1$ and $\alpha = 3/2$, F_1 , F_2 and F_3 can be written in terms of elementary functions (see Appendix A).

Here, $F_1(u)$ represents the spherical contribution to $\Phi(\mathbf{u})$, i.e., $C F_1(u) = 4\pi G \delta_c \rho_{\text{crit}} R_0^2 F_1(u)$ is nothing but the gravitational potential for the case of the spherical density profile (Makino, Sasaki & Suto 1998; Suto, Sasaki & Makino 1998). F_2 represents another spherical contribution that has arisen due to the volume changes of the perturbed ellipsoidal density profiles from the spherical ones, while F_3 represents the non-spherical deviation of $\Phi(\mathbf{u})$ from the spherical potential. If we take the equal-volume approach in performing the perturbation, then we will end up with exactly same $F_1(u)$ and $F_3(u)$ but no F_2 . Figure 1 plots these functions in a wide range of the rescaled radius u for $\alpha = 1$ and $\alpha = 3/2$. As shown, the magnitude of F_3 is an order of magnitude smaller than those of F_1 and F_2 . Since the dependence of $\Phi(\mathbf{u})$ on θ and ϕ comes from the F_3 -term (eq.[19]), it implies that $\Phi(\mathbf{u})$ is fairly insensitive to θ and ϕ . The asymptotic limit of F_3/F_1 at $u \rightarrow \infty$ has been calculated to converge to zero, which implies that the triaxial potential is almost indistinguishable from the spherical one at large distance ($u \gg 1$).

Equation (19) is valid only for $e_\sigma^2 \ll 1$. Jing & Suto (2002), however, showed that the axes ratios of cluster scale halos are typically $0.4 < c/a \leq b/a < 0.8$, which corresponds to $0.3 < e_b \leq e_c < 0.8$. To examine how well equation (19) works in this realistic range of e_σ , we integrate equation (12) numerically to obtain the real gravitational potential. Figure 2 compares the perturbative potentials (dashed lines) to the numerical results (solid lines) for various values of the halo eccentricities both in $\alpha = 1$ and $\alpha = 3/2$ cases. It is clear that the perturbative potentials agree with the numerical results excellently. We also calculate the ratios of the perturbative potentials to the numerical ones, and find the ratios less than

1.1 even for $e_b = 0.6$ and $e_c = 0.8$, which indicates that equation (19) is indeed a good approximation.

Incidentally, the gravitational potentials for the axis symmetric halos with the single eccentricity e can be also obtained from equation (19):

$$\Phi(\mathbf{u}) \approx C \left[F_1(u) \pm \frac{e^2}{2} \{ F_2(u) + \cos^2 \theta F_3(u) \} \right], \quad (23)$$

where the positive and the negative signs in front of $e^2/2$ correspond to the oblate [$a = b > c$, $e = \sqrt{1 - (c/a)^2}$] and the prolate [$a < b = c$, $e = \sqrt{1 - (a/b)^2}$] cases, respectively. Note that z -direction is always chosen as the symmetric axis in the above expression.

3.3. Iso-Potential Surfaces and Potential Profiles

Strictly speaking, the iso-potential surfaces of ellipsoidal dark halos are not necessarily exact ellipsoids (Binney & Tremaine 1987). However, we have found that the iso-potential surfaces are still best well approximated as ellipsoids (see also Figs.4 and 5 below). Thus, we model the iso-potential surfaces as triaxial ellipsoids with the rescaled major axis length, ξ , and the two eccentricities, ϵ_b and ϵ_c :

$$\xi^2 \equiv \frac{1}{R_0^2} \left(x^2 + \frac{y^2}{1 - \epsilon_b^2} + \frac{z^2}{1 - \epsilon_c^2} \right) = \text{const.} \quad (24)$$

If equation (24) is a good and consistent approximation for the real iso-potential surfaces in the frame of our perturbative approach, we should be able to find the potential profile, $\tilde{\Phi}$, that satisfies $\Phi(\mathbf{u}) = \tilde{\Phi}(\xi)$. To find a functional form of $\tilde{\Phi}$, we first expand equation (24) assuming $\epsilon_\sigma^2 \ll 1$:

$$\xi = u \left(1 + \frac{\epsilon_b^2 y^2 + \epsilon_c^2 z^2}{2r^2} \right) = u \left(1 + \frac{\epsilon_b^2 \sin^2 \theta \sin^2 \phi + \epsilon_c^2 \cos^2 \theta}{2} \right). \quad (25)$$

Substituting equation (25) into $\tilde{\Phi}(\xi)$, and expanding to first order of ϵ_σ^2 , we have

$$\begin{aligned} \tilde{\Phi}(\xi) &\approx \tilde{\Phi} \left[u \left(1 + \frac{\epsilon_b^2 \sin^2 \theta \sin^2 \phi + \epsilon_c^2 \cos^2 \theta}{2} \right) \right] \\ &= \tilde{\Phi}(u) + \frac{\partial \tilde{\Phi}(u)}{\partial u} u \frac{\epsilon_b^2 \sin^2 \theta \sin^2 \phi + \epsilon_c^2 \cos^2 \theta}{2}. \end{aligned} \quad (26)$$

Comparing equation (19) with equation (26) indicates that the functional form of $\tilde{\Phi}$ is

$$\tilde{\Phi}(\xi) = C \left[F_1(\xi) + \frac{e_b^2 + e_c^2}{2} F_2(\xi) \right], \quad (27)$$

and that the eccentricities of iso-potential surfaces ϵ_σ^2 are written in terms of their halo eccentricities e_σ^2 as

$$\frac{\epsilon_\sigma^2}{e_\sigma^2} = \frac{F_3(u)}{u\partial_u F_1(u)} = \frac{(\alpha - 2)F_3(u)}{1 - (\alpha - 2)F_1(u) - u^{2-\alpha}(1 + u)^{\alpha-2}}. \quad (28)$$

Note that ϵ_σ for the gravitational potential depends on u unlike the constant e_σ for the adopted dark matter halo profile. Figure 3 plots ϵ_σ/e_σ as a function of u for $\alpha = 1$ and $\alpha = 3/2$ cases. The $\alpha = 1$ case has a higher ratio of ϵ_σ to e_σ than the $\alpha = 3/2$ case. In the whole range of u , ϵ_σ/e_σ is less than unity, and decreases mildly as u increases.

4. GAS DENSITY AND TEMPERATURE PROFILES

In §2, we showed that the gravitational potential of dark halos is the central quantity for the hydrostatic intra-cluster gas distribution, and that the gas iso-density and temperature surfaces coincide with the halo iso-potential surfaces. Thus, one can restate every feature of the iso-potential surfaces found in §3 in terms of the iso-density surfaces of the intra-cluster gas: the iso-density and temperature surfaces of the intra-cluster gas in triaxial dark halos are approximately triaxial ellipsoids whose eccentricities are related to that of the underlying halos via equation (28), decreasing with radial distance.

Note that we have derived equation (28) using three different approximations: the first order approximation of the gravitational potential with the perturbation expansion (eq.[19]); the approximation of the iso-potential surfaces with triaxial ellipsoids (eq.[24]); the first order approximation of the iso-potential surface eccentricities with the perturbation expansion (eq.[26]). The accuracy of equation (28) depends on the accumulated errors from the three approximations. In §3.2, we have already shown that equation (19) is an excellent approximation within the 10% error.

Figure 4 plots the 2D contours of the gas iso-density surfaces (solid lines) and the ellipsoidal approximations (dot-dashed lines) on the equatorial plane ($\theta = \pi/2$) at three different radii $r = 0.1R_0, R_0$ and $10R_0$ for the given halo eccentricities $e_b = 0.6$ and $e_c = 0.8$. The contours of the gas iso-density surfaces are found numerically directly from the gravitational potential given as equation (12). We also plot the 2D shapes of the underlying halos (dashed lines) on the equatorial plane, and the circles (dotted lines) as well for reference. Figure 4 shows that the approximation of the gas density surfaces (or equivalently, the iso-potential surfaces) as ellipsoids work quite well even for large halo eccentricities $e_b = 0.6$ and $e_c = 0.8$. It also demonstrates explicitly that the intra-cluster gas is more spherical in the outer part than in the inner part of the potential, and that it is overall more spherical than

the underlying dark halo. This is intuitively understood because the potential represents the overall average of the local density profile, and also because the gas pressure is isotropic unlike the possible anisotropic velocity ellipsoids for collisionless dark matter. This fact has been also detected by hydrodynamic simulations (e.g., see Fig. 4 in Yoshikawa, Taruya, & Suto 2001).

Figure 5 plots the same as Figure 4 but for the case of halo eccentricities, $e_b = 0.8$ and $e_c = 0.8$. It shows clearly that the ellipsoidal approximations (dot-dashed lines) still work fairly well but that there are some noticeable difference between the perturbative (solid lines) and the numerical (dot-dashed lines) results. To quantify the difference of the ellipsoidal approximations of equation (28) to the gas iso-density surfaces, we measure the eccentricities of the gas iso-density surfaces directly from the contours of the numerically calculated gravitational potential, and determine the ratios between these numerical eccentricities ϵ_σ^{num} and analytical approximations ϵ_σ^{per} . Figures 6 and 7 show the results as functions of the halo eccentricities. Note that ϵ_b^{num} depends on both e_b , and e_c , so that $\epsilon_b^{num} \neq \epsilon_b^{per}$ even when $e_b = 0$ if $e_c \neq 0$. In contrast, for the analytical approximations of equation (28), ϵ_b depends only on e_b . Figures 6 and 7 also suggest that $\epsilon_b^{num}/\epsilon_b^{per}$ is not so sensitive to the values of u and α . On the whole, the values of $\epsilon_b^{num}/\epsilon_b^{per}$ are less than 1.2, indicating that the error involved in approximating ϵ_b^{num} to ϵ_b^{per} is less 20% at most. Furthermore, to the approximation error, we provide the following fitting formula to $\epsilon_b^{num}/\epsilon_b^{per}$:

$$\frac{\epsilon_b^{num}}{\epsilon_b^{per}} = 1 + [0.1 + 0.05 \log(1 + u)]e_c^3 + [0.2 + 0.03 \log(1 + u)]e_b^3, \quad (29)$$

$$\frac{\epsilon_c^{num}}{\epsilon_c^{per}} = 1 + [0.1 + 0.09 \log(1 + u)]e_b^3 + [0.2 + 0.03 \log(1 + u)]e_c^3. \quad (30)$$

Equations (29) and (30) represent the accuracy of equation (28), quantifying the calculation errors accumulated from all the above three approximations made in the derivation of equation (28). In summary, equation (28) is accurate within 10% errors for $e_\sigma < 0.6$, while within 20% errors for $e_\sigma < 0.8$.

By equations (3),(6) and (19), we obtain the density and temperature profiles for both the isothermal and the polytropic gases in the triaxial dark halos, and plot the final results in Figure 8 for $\alpha = 1$ and $\alpha = 3/2$ cases. For this figure, we choose $e_b = 0.6, e_c = 0.8$, $\gamma = 1.15$, and $(1 - \gamma)/(K_0\gamma) = 1$. For comparison, we also plot the axis-symmetric (both oblate and prolate with $e = 0.8$) and the spherical cases.

Both in isothermal and polytropic cases, the significant deviation of the resulting profiles from the sphericity are manifest especially in the range of $r \geq R_0$, increasing with r . The $\alpha = 3/2$ case shows non-negligible deviations even for $r \leq 10^{-1}R_0$. It is interesting to note that the oblate and prolate profile curves are symmetric about the spherical ones This is due

to the fact that the gravitational potentials for the oblate and the prolate halos differ only by the sign before the non-spherical perturbative term when the z -direction is chosen as the symmetric axis (see §3.1).

5. CONCLUSIONS AND DISCUSSION

We have adopted the triaxial halo density profile suggested by Jing & Suto (2002), and calculated the halo gravitational potential by using perturbation, assuming the small eccentricities of the underlying halo. The approximations have been shown to be valid even for the halos with fairly large eccentricities. With the resulting halo potentials, we found the solutions to the hydrostatic equilibrium gas equations both for the isothermal and polytropic gases. The corresponding gas density and temperature profiles have been shown to deviate from the conventional spherical models significantly at large radial distances.

We have also derived a useful analytical formula for the eccentricity ratio between the gas and the halo as a function of radial distance. It has been shown that the intra-cluster gas is rounder than the underlying halo, and that the gas eccentricity decreases with radial distance. It provides a quantitative explanation about why the gas inside dark matter halos are observed to be less elongated than the halo themselves in hydrodynamic simulations. We expect wide applications of this formula: First, it can be applied to clusters to determine the shapes of the unseen dark halos from the observed shapes of the intra-cluster gas from the X-ray and Sunyaev-Zel'dovich effects. Second, it can be used to reduce the errors involved in the measurement of the Hubble constant caused by the cluster asphericity. Third, it can be also useful in determining cosmic shear from the weak gravitational lensing surveys, and so on.

It is worth emphasizing that our analytical results are not empirical fitting formula, but derived from the first principles using the perturbation theory. The only assumptions made in our derivation is that the intra-cluster gas is in hydrostatic equilibrium. Thus, it will be also possible to test the validity of hydrostatic equilibrium of the intra-cluster gas model using our analytical results. Furthermore, our results are quite general in the sense that they are derived for any arbitrary value of the gas constants, γ and K_0 , and thus can be used to constrain the values of γ and K_0 through the direct comparison with the observational data.

We thank A. Taruya, M. Oguri, and T. Kuwabara for their useful comments. We also thank the anonymous referee for careful reading of the original manuscript and many helpful suggestions. J. L. gratefully acknowledges the support from the JSPS fellowship.

This research was supported in part by the Grant-in-Aid for Scientific Research of JSPS (12640231, 14102004, 14-02038).

A. Analytic Expressions for $\alpha = 1$ and $\alpha = 3/2$ cases

For the inner spectral indices of $\alpha = 1$ and $\alpha = 3/2$, which are indeed suggested from numerical simulations, F_i and ϵ_σ/e_σ defined in §3 can be written explicitly in terms of elementary functions. We provide their expressions here which may be useful in quantitative confrontation of our results with observations.

For $\alpha = 1$,

$$F_1(u) = -\frac{1}{u} \ln(1+u), \quad (\text{A1})$$

$$F_2(u) = -\frac{1}{3} + \frac{2u^2 - 3u + 6}{6u^2} + \left(\frac{1}{u} - \frac{1}{u^3}\right) \ln(1+u), \quad (\text{A2})$$

$$F_3(u) = \frac{u^2 - 3u - 6}{2u^2(1+u)} + \frac{3}{u^3} \ln(1+u), \quad (\text{A3})$$

$$\frac{\epsilon_\sigma^2}{e_\sigma^2} = \frac{6(1+u) \ln(1+u) + u^3 - 3u^2 - 6u}{2u^2[(1+u) \ln(1+u) - u]}. \quad (\text{A4})$$

For $\alpha = 3/2$,

$$F_1(u) = -2 + 2\sqrt{\frac{1+u}{u}} - \frac{2}{u} \ln(\sqrt{u} + \sqrt{1+u}), \quad (\text{A5})$$

$$F_2(u) = \frac{4}{3} + \left(\frac{5}{4u^3} + \frac{5}{12u^2} - \frac{13}{6u} - \frac{4}{3}\right) \sqrt{\frac{u}{1+u}} + \left(\frac{2}{u} - \frac{5}{4u^3}\right) \ln(\sqrt{u} + \sqrt{1+u}), \quad (\text{A6})$$

$$F_3(u) = -\left(\frac{15}{4u^3} + \frac{5}{4u^2} - \frac{1}{2u}\right) \sqrt{\frac{u}{1+u}} + \frac{15}{4u^3} \ln(\sqrt{u} + \sqrt{1+u}), \quad (\text{A7})$$

$$\frac{\epsilon_\sigma^2}{e_\sigma^2} = \frac{(15 - 5u - 2u^2) \sqrt{u/(1+u)} - 15 \ln(\sqrt{u} + \sqrt{1+u})}{8u^3 \sqrt{u(1+u)} - 8u^2 \ln(\sqrt{u} + \sqrt{1+u})}. \quad (\text{A8})$$

REFERENCES

- Allen, S.W., Schmidt, R.W., & Fabian, A.C. 2002, MNRAS, in press (astro-ph/0111368)
- Audit, E., Teyssier, R., & Alimi, J. M. 1997, A&A, 325, 439
- Binney, J., & Tremaine, S. 1987, Galactic Dynamics (Princeton: Princeton Univ. Press)
- Birkinshaw, M. 1999, Phys. Rep., 310, 97
- Birkinshaw, M., Hughes, J. P., Arnaud, K. A. 1991, ApJ, 379, 466
- Buote, D. A. & Canizares, C. R. 1994, ApJ, 427, 86
- Buote, D.A., Jelema, T.E., Canizares, C.R., & Garmire, G.P. 2002, ApJ, in press (astro-ph/0205469)
- Fox, D. C., & Pen, U. L. 2002, ApJ, 574, 38
- Fukushiege, T., & Makino, J. 1997, ApJ, 477, L9
- Hughes, J.P., & Birkinshaw, M. 1998, ApJ, 501, 1
- Inagaki, Y., Suginoara, T. & Suto, Y. 1995, PASJ, 47, 411
- Jeffreys, H. 1976, The Earth (London :Cambride Univ. Press) 6th ed.
- Jenkins, A., Frenk, C.S., White, S.D.M., Colberg, J.M., Cole, S., Evrard, A.E., Couchman, H.M.P. & Yoshida, N., 2001, MNRAS, 321, 372
- Jing, Y. P., & Suto, Y. 2000, ApJ, 529, L69
- Jing, Y. P., & Suto, Y. 2002, ApJ, 574, 538
- Komatsu, E. et al. 2001, PASJ, 53, 57
- Komatsu, E. & Seljak, U. 2001, MNRAS, 327, 1353
- Lee, J. & Shandarin, S.F. 1998, ApJ, 500, 14
- Lee, J. & Shandarin, S.F. 1999, ApJ, 517, L5
- Markevitch, M., Forman, W. R., Sarazin, C. L., & Vikhlinin, A. 1998, ApJ, 503, 77
- Makino, N., & Sasaki, S., & Suto, Y. 1998, ApJ, 497, 555
- Monaco, P. 1995, ApJ, 447, 23

- Moore, B., & Governato, F., Quinn, T., & Stadel, J., Lake, G. 1998, ApJ, 499, L5
- Navarro, J. F., & Frenk, C. S., & White, S.D.M. 1996, ApJ, 462, 563
- Navarro, J. F., & Frenk, C. S., & White, S.D.M. 1997, ApJ, 490, 493
- Romanowsky, A. J. & Kochanek, C. S. 1998, ApJ, 493, 641
- Sheth, R. K., & Tormen, G. 1999, MNRAS, 308, 119
- Suto, Y., Sasaki, S., & Makino, N. 1998, ApJ, 509, 544
- Yoshikawa, K., Itoh, M. & Suto, Y. 1998, PASJ, 50, 203
- Yoshikawa, K., Taruya, A. & Suto, Y. 2001, ApJ, 558, 520

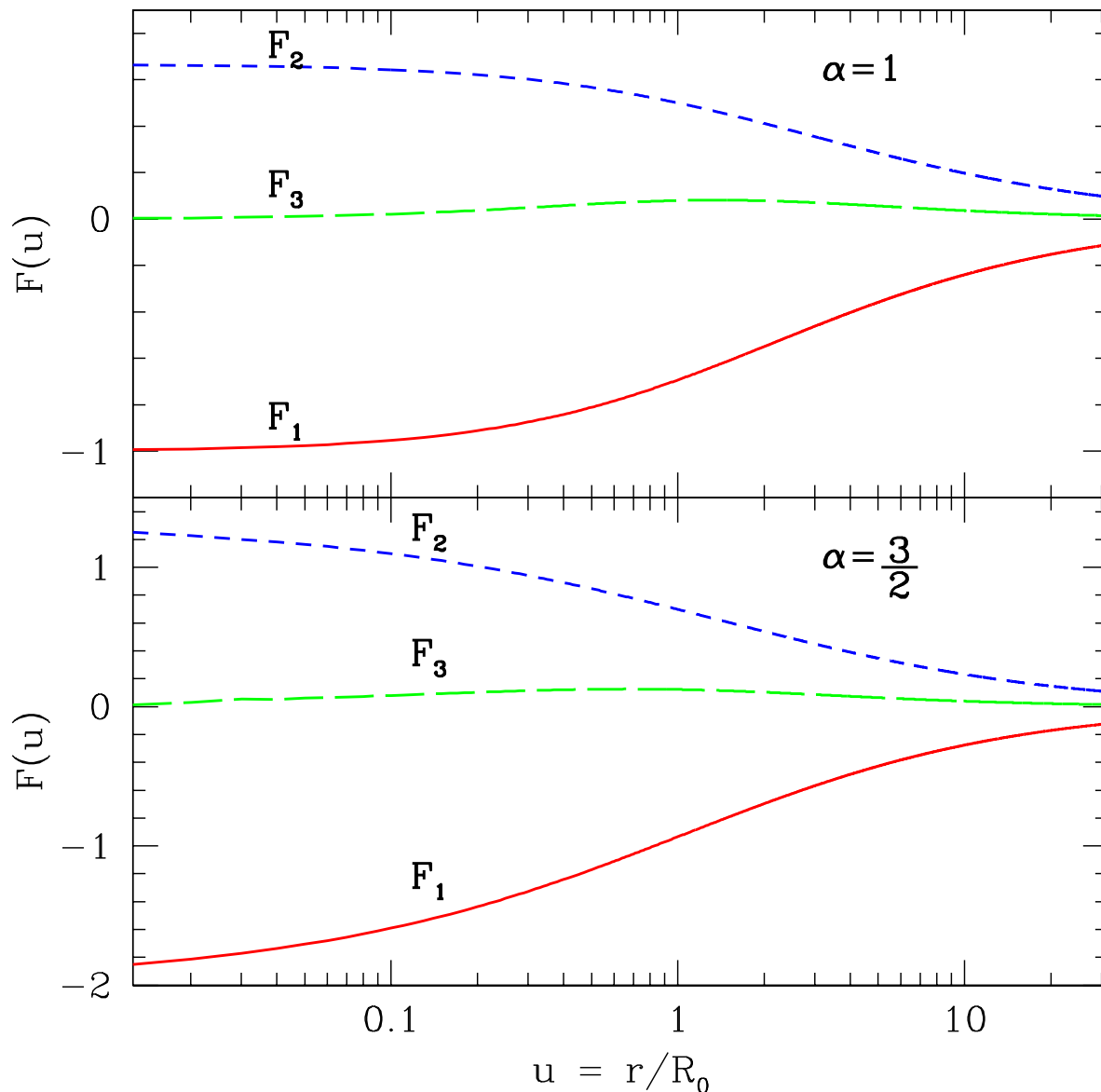


Fig. 1.— The behavior of the three functions, F_1, F_2 and F_3 (solid, dashed, and long-dashed lines, respectively) given in the perturbative result of the gravitational potential (eqs.[20],[21] and [22]). *Upper Panel:* it corresponds to the case where the inner slope of the halo density profile defined in equation (9) has the value of $\alpha = 1$. *Lower Panel:* it corresponds to $\alpha = 3/2$.

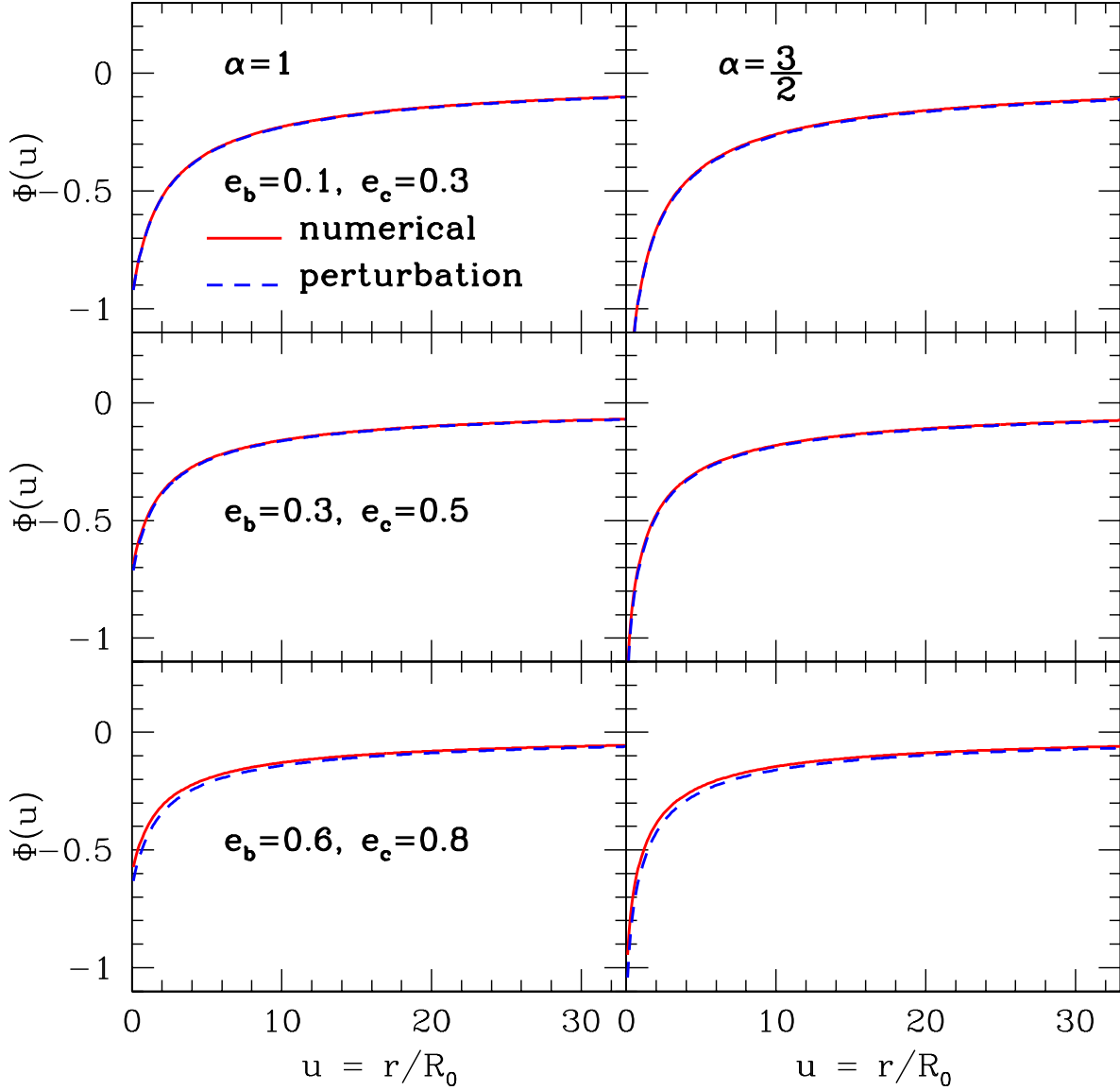


Fig. 2.— Comparison of the numerical gravitational potentials (solid lines) with the perturbative results (dashed lines) on the equatorial plane of $\theta = \frac{\pi}{2}$ and $\phi = 0$. *Top*: it correspond to the case where the underlying halo has the eccentricities, $e_b = 0.1, e_c = 0.3$. *Middle*: $e_b = 0.3, e_c = 0.5$. *Bottom*: $e_b = 0.6, e_c = 0.8$. The left and right panels correspond to $\alpha = 1$ and $\alpha = 3/2$, respectively.

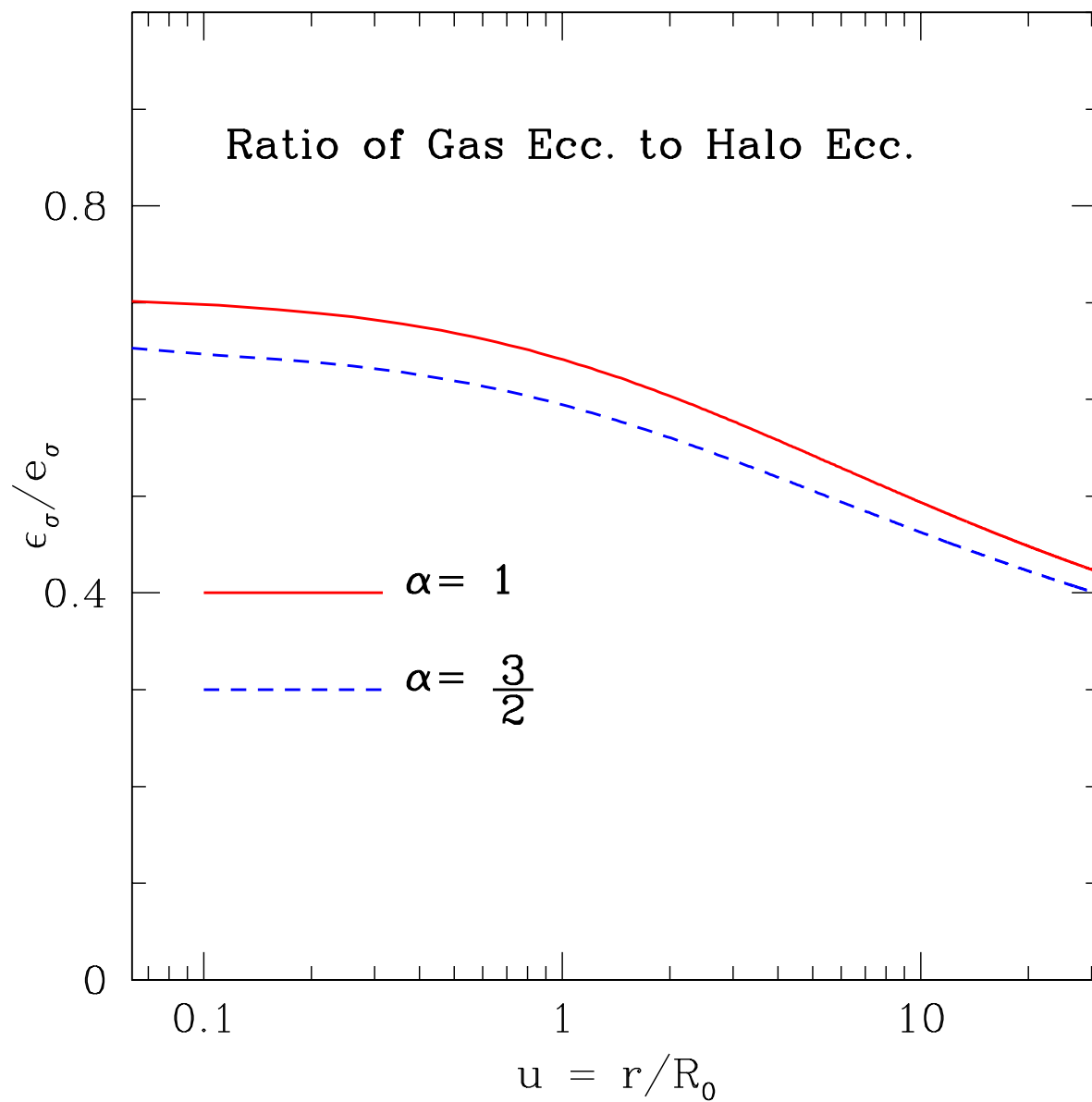


Fig. 3.— The ratio of the eccentricity of the iso-potential surface to that of the halo iso-density surface from the perturbative result (28); $\alpha = 1$ (solid line) and $\alpha = 3/2$ (dashed line).

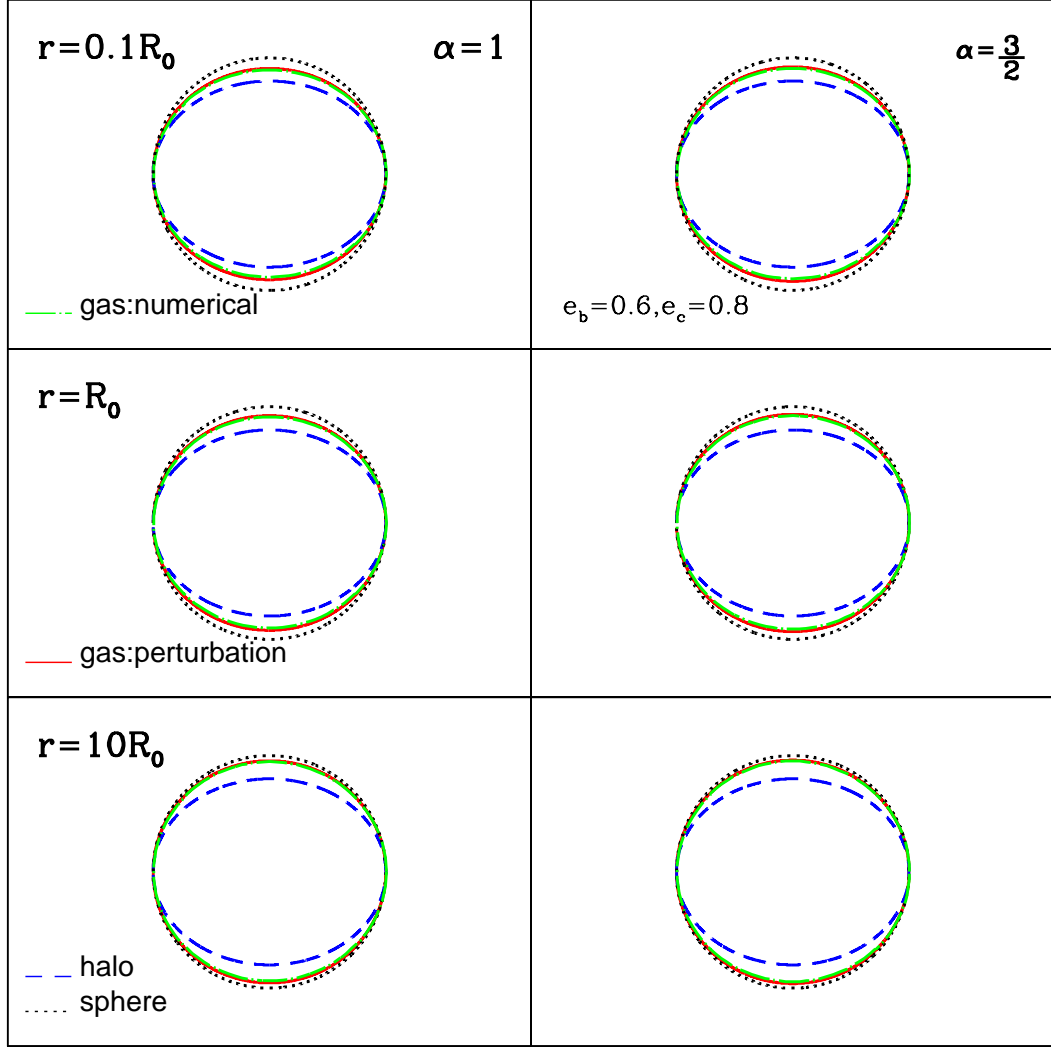


Fig. 4.— The shapes of the iso-density surfaces of the gas embedded in the halo with the eccentricities $e_b = 0.6$ and $e_c = 0.8$ at three different radii, $r = 0.1R_0, R_0$ and $10R_0$ on the equatorial plane ($\theta = \pi/2$). The sizes of the curves are arbitrary. In each panel, the solid and the dot-dashed lines represent the numerical and the perturbative results of the gas density profile, respectively. While the dashed lines represent the halo iso-density surfaces. The dotted circles are also plotted for comparison.

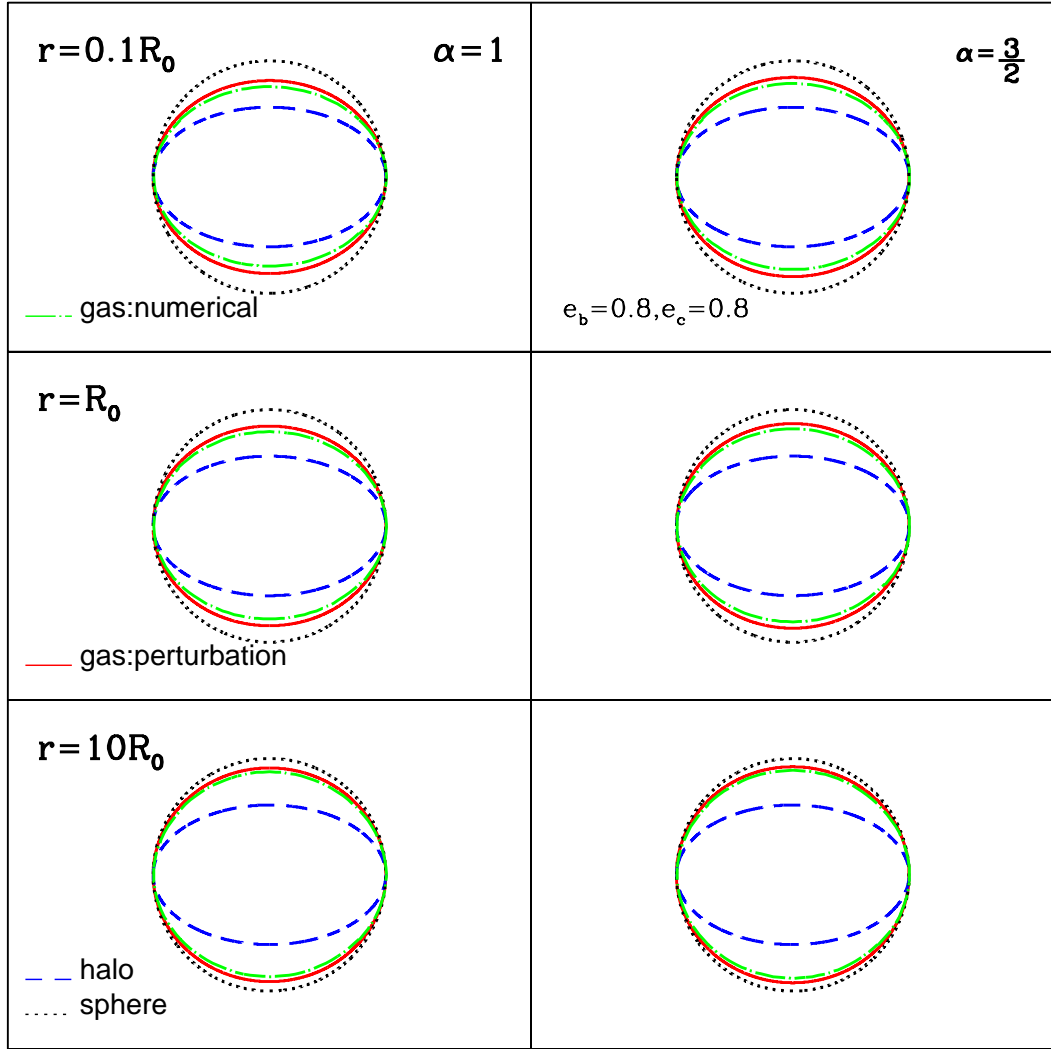


Fig. 5.— Same as Figure 4, but for larger halo eccentricities, $e_b = 0.8$ and $e_c = 0.8$.

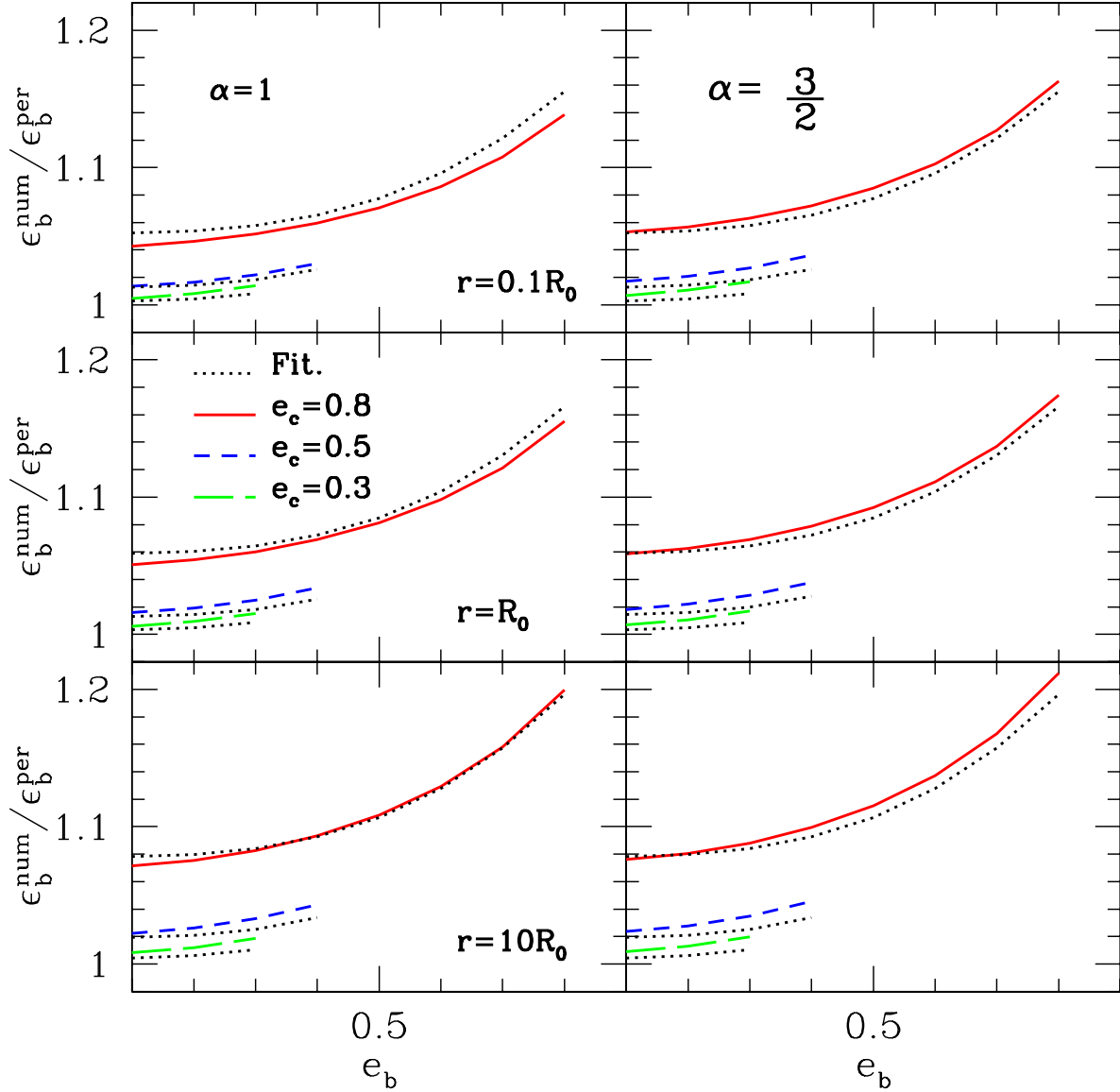


Fig. 6.— The ratio between the gas eccentricity fitted to the numerical results and the perturbative ones as a function of the halo eccentricity e_b . In each panel, the solid, the dashed and the long-dashed lines represent the cases of $e_c = 0.8, 0.5$ and 0.3 , respectively. The dotted line represents the fitting formula given in equations (29) and (30).

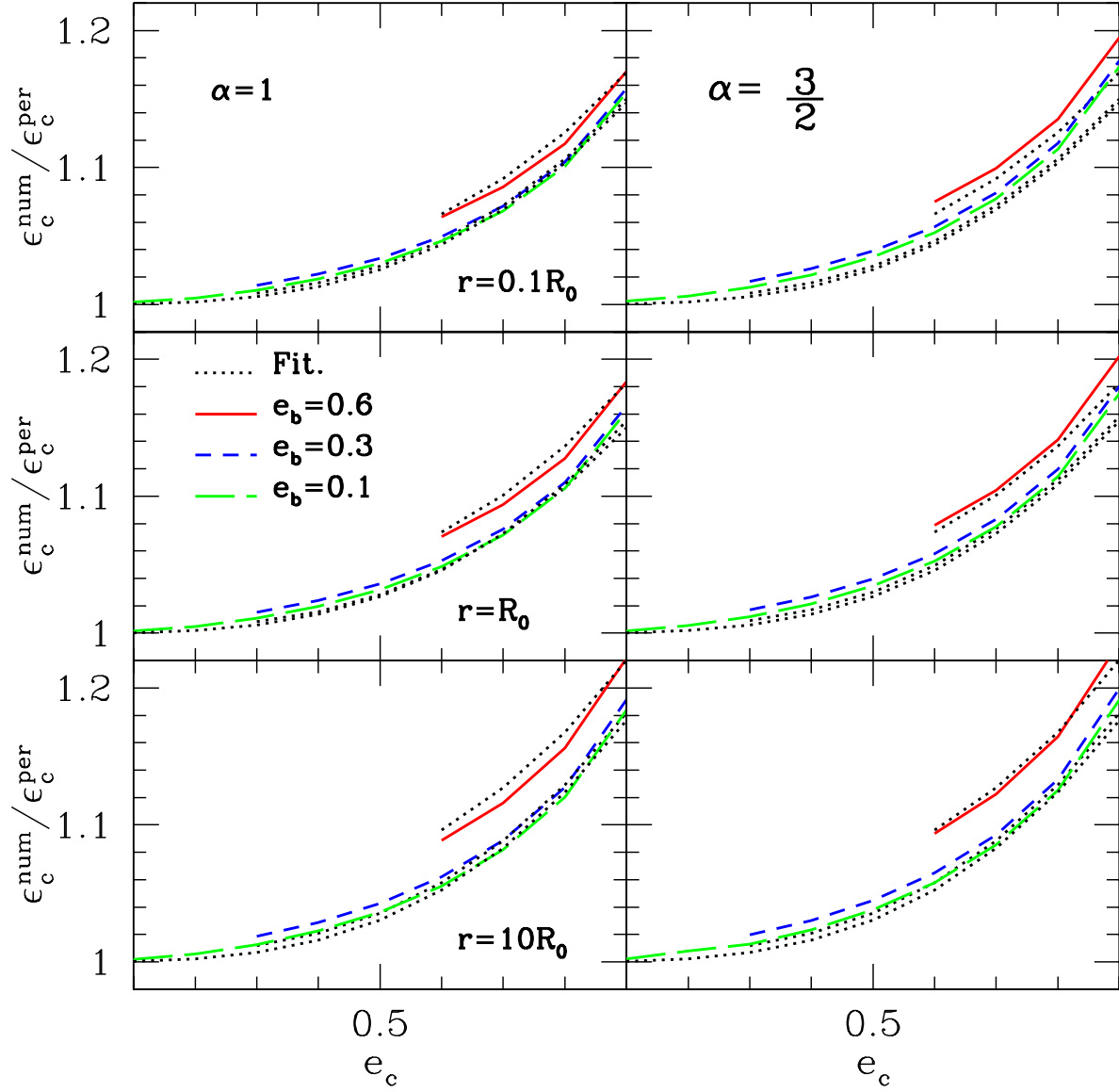


Fig. 7.— Same as Figure 6, but as a function of e_c for the three different values of $e_b = 0.1, 0.3$ and 0.6 .

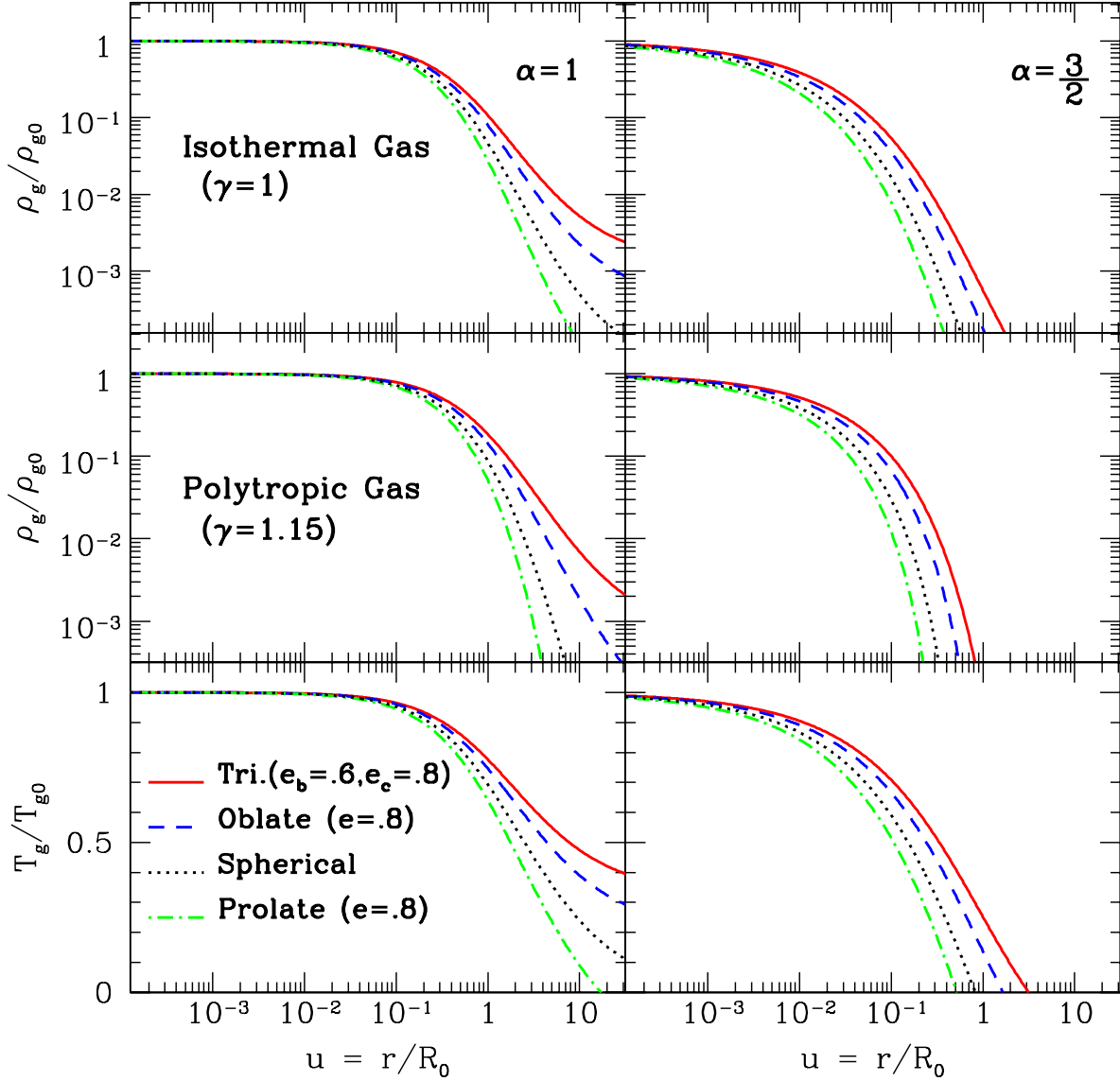


Fig. 8.— The hydrostatic equilibrium solutions for the intra-cluster gas distribution. *Top:* the density profiles of the isothermal gas. *Middle:* the density profiles of the polytropic gas with the polytropic index of $\gamma = 1.15$. *Bottom:* the temperature profiles of the polytropic gas. In each panel, the solid, the dashed, the dotted, and the dot-dashed lines represent the gas profiles for the triaxial ($e_b = 0.6, e_c = 0.8$), the oblate ($e = 0.8$), the spherical, and the prolate ($e = 0.8$) halo cases, respectively.